



Highly efficient removal of bisphenol A by a three-dimensional graphene hydrogel-AgBr@rGO exhibiting adsorption/photocatalysis synergy

Fangyuan Chen, Weijia An, Li Liu, Yinghua Liang, Wenquan Cui*

College of Chemical Engineering, Hebei Key Laboratory for Environment Photocatalytic and Electrocatalytic Materials, North China University of Science and Technology, Tangshan 063009, PR China



ARTICLE INFO

Article history:

Received 13 March 2017

Received in revised form 12 May 2017

Accepted 27 May 2017

Available online 29 May 2017

Keywords:

AgBr

rGH-AgBr@rGO

Adsorption/photocatalysis synergy

ABSTRACT

The increasing extent of environmental pollution by industrial chemicals necessitates the development of facile methods of their removal. Among the various techniques employed for this purpose, photocatalytic degradation is particularly attractive, since it does not require the use of other chemicals, achieving pollutant mineralization by the action of light and atmospheric oxygen only. However, most photocatalysts suffer from poor stability and recyclability, which limits their practical applications. This study describes the encapsulation of AgBr by reduced graphene oxide to form a composite (AgBr@rGO) that can be incorporated into graphene to form hydrogels (rGH-AgBr@rGO) with three-dimensional (3D) network structures. The core-shell structure of AgBr@rGO inhibited the growth of AgBr particles, achieving excellent control over their size (500–600 nm), while hybridization with graphene promoted the rapid migration and separation of photogenerated charges. Bisphenol A (BPA) were rapidly adsorbed by the 3D graphene nanosheets of rGH-AgBr@rGO and promptly degraded by AgBr@rGO nanoparticles under visible-light irradiation, showing that the synergy between adsorption and photocatalytic degradation could significantly improve pollutant removal efficiency. Moreover, the micron-sized 3D mesh structure could be regenerated using a simple filter without the need for a complex catalyst filtration system. The obtained results revealed a superior synergy between photocatalytic and adsorption-based pollutant degradation by rGH-AgBr@rGO, which achieved a 1.5-fold higher BPA removal degree than pure AgBr, exhibiting values above 90% after five consecutive cycles. Finally, the degree of BPA degradation was maintained at 100% during the first 6 h under continuous flow conditions.

© 2017 Elsevier B.V. All rights reserved.

1. Introduction

Silica [1], organic [2], and graphene hydrogels [3] exhibit high surface areas, large pore volumes, and good heat resistance, providing excellent adsorption properties and selectivity for catalytic applications. Graphene hydrogels (rGH) feature three-dimensional (3D) porous networks (held together by π - π interactions and hydrogen bonding) with high specific surface areas ($\sim 512 \text{ m}^2/\text{g}$) [4], low densities ($\sim 3.6 \text{ mg}/\text{cm}^3$) [5], and well-developed interpenetrating pore structures. 3D-assembled rGH macrostructures exhibit new collective physicochemical properties together with excellent adsorption capability and recyclability [4,6], being poten-

tially applicable for adsorption and removal of organic pollutants [7], marine oil spills [8], and heavy metal ions [9,10].

Photocatalysis is an effective way of degrading organic pollutants with the help of photogenerated electrons and holes [11,12]. Common photocatalysts such as TiO_2 , ZnO , Ag_3PO_4 , and AgX ($\text{X}=\text{Cl}$, Br , I) exhibit low separation efficiencies and high recombination rates of photogenerated charges, which limits further activity improvement. Graphene features a conductive π - π conjugated structure, exhibiting high single-layer charge mobility ($2 \times 10^5 \text{ cm}^2/(\text{Vs})$) [13] and good conductivity ($1 \times 10^2 \text{ S}/\text{m}$). Hence, combining highly conductive graphene with photocatalysts enables the charge separation efficiency to be further improved.

Bera et al. [14] combined CdS nanoparticles (zero-dimensional), CdS nanorods (one-dimensional), and CdS nanosheets (two-dimensional) with reduced graphene oxide (rGO) sheets to form hybrid structures exhibiting variable catalytic activity, with graphene playing an important role in rapid electron transfer. In

* Corresponding author.

E-mail address: wk cui@163.com (W. Cui).

addition, other graphene-grafted semiconductors (e.g., ZnWO_4 [15] and ZnO [16]) were reported in Zhu's works, achieving inhibition of light-induced corrosion and improved catalyst activity/stability. These studies revealed that graphene significantly enhances rapid charge conduction and photocatalytic activity and exerts a very large effect on photocatalytic performance. The above investigations mainly focused on powdered catalysts with low specific surface areas, which often limited their adsorption capacity and frequently necessitated the use of complex filtering systems for recycling.

Recycling efficiency can be improved by loading photocatalyst onto 3D graphene hydrogels, making use of the abovementioned collective physicochemical properties. In our previous work [17], TiO_2 was combined with rGO to form a mixed hydrogel (TiO_2 -rGH), whose unique 3D structure and abundant channels improved the adsorption rate and adsorption capacity. TiO_2 nanoparticles loaded on the hydrogel could in-situ rapid adsorption on graphene nanosheets of Cr (VI) on the photocatalytic reduction, achieving synergistic adsorption-based and photocatalytic removal of contaminants. TiO_2 was also loaded onto a 3D polyaniline (PANI) [18] hydrogel to prepare the corresponding composite, which showed a photocurrent 28 times higher than that of pristine TiO_2 . This observation implied that the presence of PANI increased the separation rate of photogenerated charges, successfully achieving in situ photocatalytic degradation of organic contaminants due to their enhanced adsorption. Liu et al. [19] used a one-step hydrothermal method to prepare a highly stable BiOBr/rGO composite aerogel, which could be easily recovered from reaction mixtures, maintaining high activity and showing negligible catalyst loss. Cui et al. [20] used in situ precipitation to prepare Ag_3PO_4 /graphene hydrogel composites that showed photocurrents of $2.5 \mu\text{A cm}^{-2}$ after 25 min irradiation with visible light, exhibiting higher photoelectric conversion efficiencies and stabilities than pristine Ag_3PO_4 . Thus, graphene hydrogel-based hybrid structures can not only improve the photocatalytic activity of AgX , but also enhance their stability. However, in existing reports, only powdered catalysts were loaded on 3D hydrogels, with the increased difficulty of hybridizing graphene nanosheets and photocatalyst nanoparticles limiting photocatalytic property improvement.

Hence, in this work, AgBr/rGO hybrid was synthesized by coating graphene nanosheets with AgBr using a precipitation method, which not only inhibited AgBr photocorrosion, but also increased the separation rate of photogenerated charges. Furthermore, loading AgBr/rGO nanoparticles onto a graphene hydrogel resulted in the formation of a 3D network structure ($\text{rGH-AgBr}/\text{rGO}$) with enhanced surface adsorption properties that promoted fast adsorption of organic pollutants, while the loaded AgBr/rGO nanoparticles enabled their rapid degradation. As an example, the synergy of in situ adsorption and visible-light-induced catalytic degradation significantly improved the removal efficiency of bisphenol A (BPA). The developed micron-scale hybrid material could be recycled using a simple filter, not requiring complex catalyst recovery filtration systems.

2. Experimental

2.1. Synthesis of $\text{rGH-AgBr}/\text{rGO}$

2.1.1. Synthesis of graphene oxide

Graphene oxide (GO) was prepared using a modified Hummers' method [17]. Graphite (1.5 g, 325 mesh) was mixed with ice-cold H_2SO_4 (35 mL) over 10 min, followed by addition of NaNO_3 (0.75 g) and KMnO_4 (4.5 g) and stirring for 3 h at $T \leq 20^\circ\text{C}$ and for another 3 h at $T = 40^\circ\text{C}$. Subsequently, water (100 mL) was added, and the temperature was increased to 90°C and maintained for 1.5 h. At

least 100 mL of deionized water and 3 mL of H_2O_2 (30 wt%) were added to the suspension during the synthetic process. The brown precipitate of GO was filtered, washed with 10% HCl, and dialyzed (36-mm (MD44) dialysis bag, molecular weight: 8000–14000) for seven days to afford pure graphene oxide.

2.1.2. Synthesis of AgBr/rGO and AgBr

A solution of silver hydroxide in ammonia was dropwise added to a small amount of ultrasonicated GO (2 mL, 0.1 mg/mL), and the mixture was stirred for 40 min. Subsequently, aqueous KBr was dropwise added, and the reaction mixture was further stirred for 3 h to afford AgBr/rGO . In the preparation of AgBr , GO was replaced with deionized water (2 mL), with other steps being the same as above.

2.1.3. Synthesis of $\text{rGH-AgBr}/\text{rGO}$

The as-prepared AgBr/rGO was mixed with GO to achieve GO loadings of 5, 7, 10, and 15 wt%. The obtained mixture was ultrasonicated for ~ 40 min, followed by addition of vitamin C (VC, 10 times the mass of GO) and 40-min ultrasonication. Subsequent heating at 95°C for 1.5 h afforded $\text{rGH-AgBr}/\text{rGO}$. The as-prepared hydrogels were washed with deionized water to remove residual ions and freeze-dried to obtain aerogels, which were denoted as 5% $\text{rGH-AgBr}/\text{rGO}$, 7% $\text{rGH-AgBr}/\text{rGO}$, 10% $\text{rGH-AgBr}/\text{rGO}$, and 15% $\text{rGH-AgBr}/\text{rGO}$.

Graphene hydrogel containing non-encapsulated AgBr (rGH-AgBr) was prepared by replacing AgBr/rGO with AgBr , the remaining steps being identical to those used for $\text{rGH-AgBr}/\text{rGO}$ synthesis.

2.2. Synthesis of pristine rGH

GO was ultrasonicated for 40 min, and a 10-fold excess of VC (by mass) was added. The reaction mixture was ultrasonicated for 1 h and further heated for 1 h at 95°C in a water bath. The as-prepared hydrogels were washed with distilled water for 3–5 times and freeze-dried to obtain aerogels.

2.3. Characterization of $\text{rGH-AgBr}/\text{rGO}$

The crystal structure of $\text{rGH-AgBr}/\text{rGO}$ was probed by X-ray diffraction (XRD) using a D MAX 2500 pc Rigaku diffractometer ($\text{Cu } K_\alpha$ radiation, working voltage=40 kV, working current=100 mA, scan range=5–80°). The morphology and size of catalyst particles were characterized by field emission scanning electron microscopy (FE-SEM; S-4800, Hitachi, Japan) and transmission electron microscopy (TEM; JEOL JEM-2010). UV-vis diffuse reflectance spectroscopy (Puxi, UV1901) was used for optical absorption measurements. Fourier transform infrared (FTIR) spectra were recorded on an IR Vertex70 FTIR spectrometer. X-ray photoelectron spectroscopy (XPS) measurements were carried out using an XSAM800 apparatus. The electrochemical performance of samples in 0.1 M Na_2SO_4 as an electrolyte was characterized using a three-electrode quartz cell and a CHI660E electrochemical workstation, with Pt foil used as a counter electrode, and a saturated calomel electrode used as a reference. Photoluminescence (PL) spectra were recorded on a Hitachi F-7000 spectrometer. The Brunauer-Emmett-Teller (BET) specific surface area of the sample was characterized by nitrogen adsorption at 77 K with a Micromeritics 3020 instrument.

2.4. Adsorption ability, synergy of adsorption and photocatalysis in BPA degradation

2.4.1. Static system

The adsorption/photocatalytic activities of as-prepared samples were measured in a multi-tube agitated reactor (XPA-7) equipped

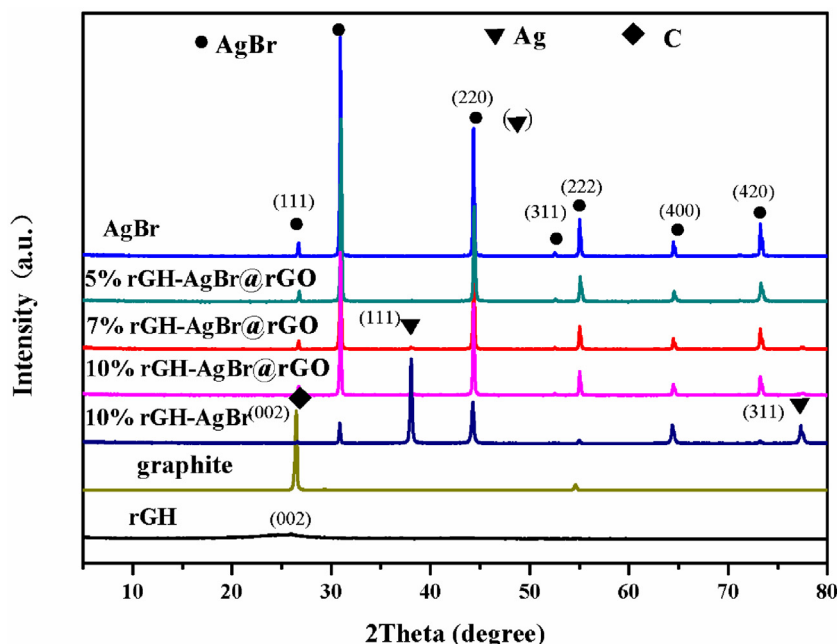


Fig. 1. XRD patterns of rGH, AgBr, graphite, and rGH-AgBr@rGO.

with a 400-W metal halide lamp as a light source, with a 420-nm-cutoff filter placed 10 cm away from an unsealed beaker filter ultraviolet light (420 nm). A glass reactor held at 25 ± 2 °C by externally circulating water was employed for the test group. In the adsorption test, equivalent amounts of catalysts (0.1 g 10% rGH-AgBr@rGO, 0.09 g AgBr, 0.01 g rGH, and 0.01 g activated carbon (AC)) were added to a solution of BPA (50 mL, 20 ppm), and 3 mL aliquots were sampled at certain time intervals and filtered through a micro-pore membrane. In the adsorption/photocatalysis test, 0.1 g samples of different catalysts were added to the BPA solution (50 mL, 20 ppm), and the obtained suspensions were magnetically stirred for 30 min to reach adsorption-desorption equilibrium prior to irradiation, with 3-mL aliquots sampled at certain time intervals. The adsorption/photocatalysis synergy test was performed similarly to the adsorption/photocatalysis test in addition to the process without adsorption-desorption equilibrium and direct light.

During cycling performance evaluation, three 0.1 g samples of 10% rGH-AgBr@rGO were added to the BPA solution (50 mL, 20 ppm) and subjected to adsorption, adsorption/photocatalysis, and adsorption/photocatalysis synergy tests. After each cycle, the catalyst was isolated by 38 μ m filtration without any other treatment, being subsequently added to a fresh BPA solution of the same volume and concentration.

BPA concentrations were detected by high-performance liquid chromatography (HPLC) using methanol/water (70/30, v/v) as the mobile phase, an elution time of 6 min, and a detector wavelength of 278 nm. A C18 reversed-phase column (Agilent 1100, 4.6 nm \times 200 nm) was used for chromatographic analysis. Prior to injection, the BPA solution was filtered through a 0.22 μ m membrane to remove any solid particles present.

2.4.2. Dynamic system

A grooved fixed-bed reactor (40 mm \times 20 mm \times 2 mm) was used to test the synergy of adsorption and photocatalysis in a dynamic system, using a 500 W xenon lamp (CHF-XW-500) as a light source and a filter assembly ($\lambda < 420$ nm) placed 5 cm away from it. rGH-AgBr@rGO (0.5 g) was immobilized inside the reactor using quartz glass and a clip to prevent leakage, reaction from the groove through the 10 ppm BPA solution. The flow rate of the BPA solu-

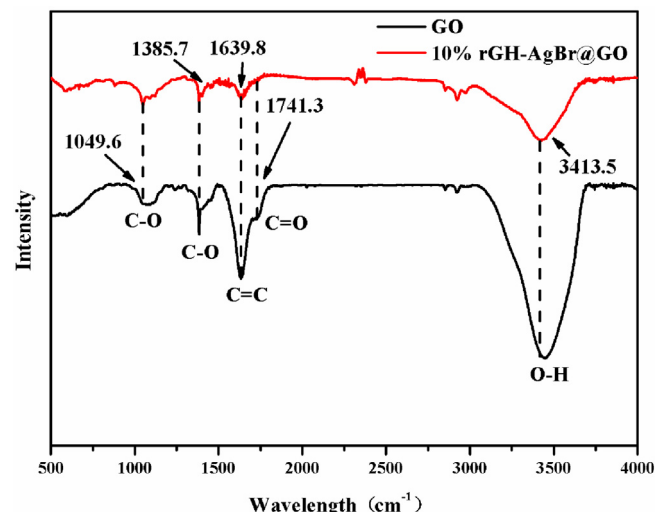


Fig. 2. FTIR spectra of GO and 10% rGH-AgBr@rGO.

tion was controlled by a peristaltic pump (YZ1515, Baoding), and 3 mL aliquots were sampled every 2 h, with the BPA concentration therein determined by HPLC.

3. Results and discussion

Fig. 1 shows XRD spectra of rGH, AgBr, graphite, and rGH-AgBr@rGO, revealing distinct characteristic peaks of rGH at 24.8°, ascribed to reflection from the (002) plane. The XRD pattern of rGH-AgBr@rGO mainly displays the diffraction peaks of AgBr at 26.7, 31.0, 44.3, 52.5, 55.0, 64.5, and 73.3°, corresponding to (111), (200), (220), (311), (222), (400), and (420) planes, respectively (JCPDS file No. 06-438) [21]. Peaks at 38.1 and 77.5° correspond to (111) and (311) planes of Ag, respectively (JCPDS file No. 04-0783) [22]. No rGH peak (24.8°) was observed for rGH-AgBr@rGO due to its low rGH content. However, a weak characteristic peak of Ag was observed for the above catalyst, attributed to the use of a large VC excess during composite hydrogel preparation. The above Ag

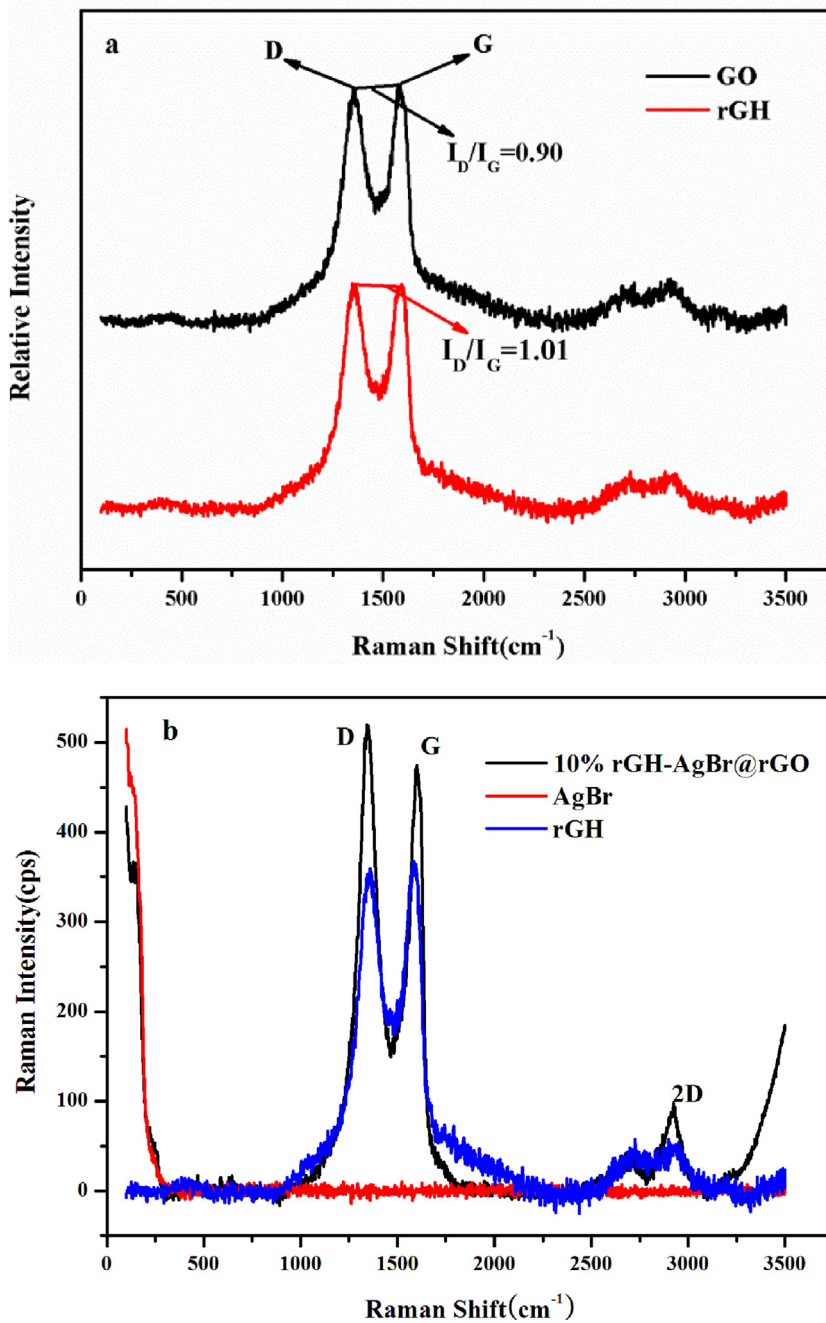


Fig. 3. Raman spectra of (a) rGH and GO and (b) 10% rGH-AgBr@rGO, rGH, and GO.

peaks were remarkably enhanced in the case of 10% rGH-AgBr, implying the reduction of AgBr to Ag in this case and revealing that AgBr in the core@shell AgBr@rGO was not reduced by VC in 10% rGH-AgBr@rGO.

FTIR spectroscopy was employed to confirm the reduction of oxygenated GO groups and detect chemical interaction between AgBr and rGO, being a powerful tool for quantitative analysis and purity determination [23]. Fig. 2 displays FTIR spectra of GO and rGH-AgBr@rGO, revealing strong characteristic GO peaks at 3413, 1741, 1639, 1385, and 1049 cm⁻¹, attributed to OH, carbonyl C=O, aromatic C=C, and alkoxy C—O stretches, respectively [24]. Compared to the case of GO, the intensities of all characteristic absorption peaks in the spectrum of rGH-AgBr@rGO were greatly reduced. In particular, the C=O peak at 1741 cm⁻¹ almost completely disappeared, indicating the complete reduction of GO

during the synthesis of the above catalyst. Moreover, absorption peaks at 3413 and 1049 cm⁻¹ were slightly shifted, implying hybridization of constituent materials.

Raman spectroscopy was further employed to determine the degree of disorder and amount of defects in rGH-AgBr@rGO. The intensity ratio of D (in 1358 cm⁻¹) and G (in 1580 cm⁻¹) bands (I_D/I_G) was used as a measure of graphene defect density, i.e., high I_D/I_G values were attributed to an increased number of sp³ defects and enhanced disorder, implying a decrease in the average size of sp² carbon islands, and hence, an increased degree of GO reduction [25]. rGH showed an I_D/I_G value of 1.01, which was higher than that of GO (0.90), confirming that reduction generated a large number of sp³ defects (Fig. 3a). Fig. 3b displays Raman spectra of 10% rGH-AgBr@rGO, rGH, and GO samples. Compared to rGH ($I_D/I_G=1.01$), rGH-AgBr@rGO showed an increased I_D/I_G value of 1.2, suggesting

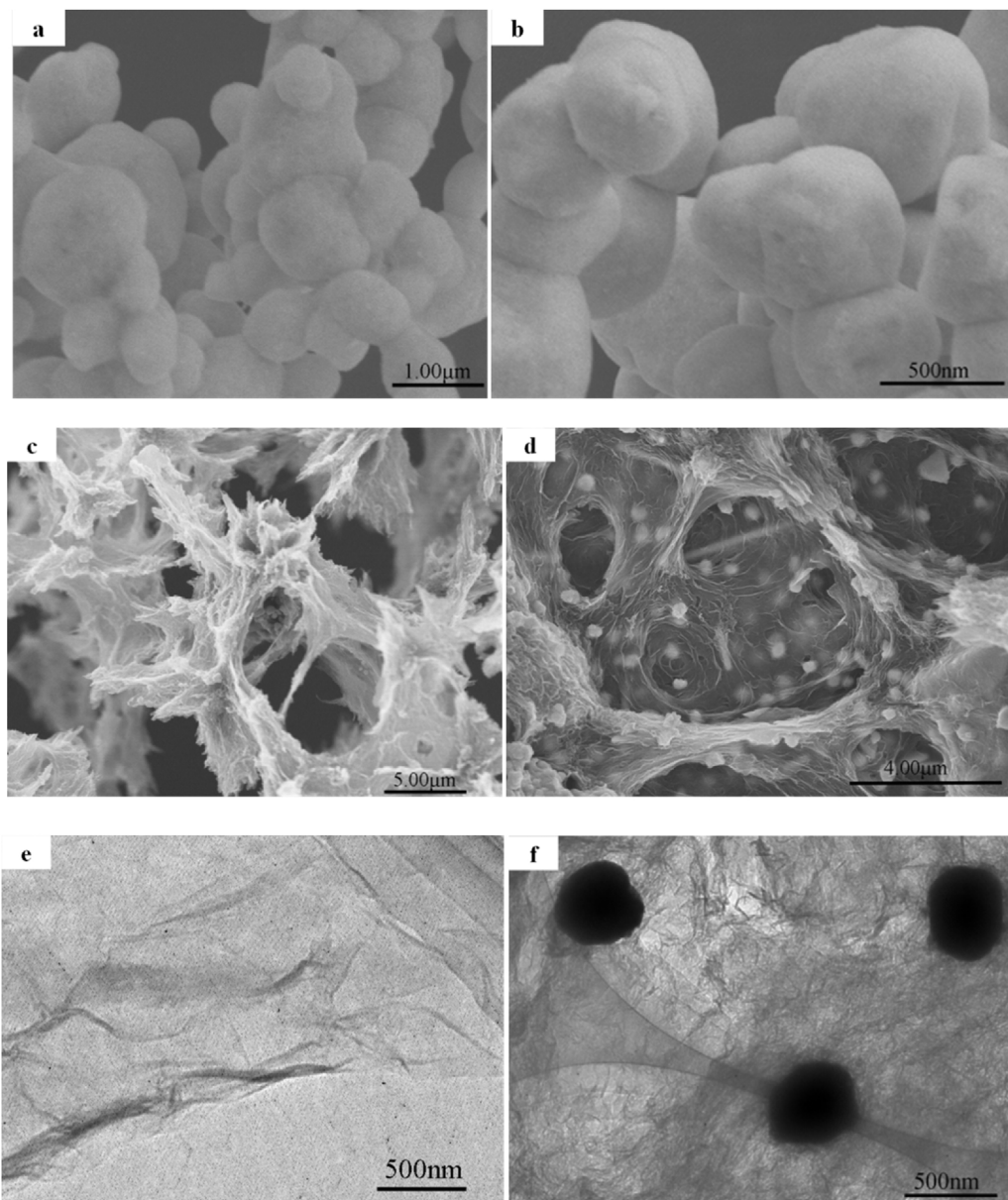


Fig. 4. SEM images of (a) pure AgBr, (b) AgBr@rGO, (c) rGH, and (d) 10% rGH-AgBr@rGO. TEM images of (e) GO and (f) 10% rGH-AgBr@rGO.

that this composite contained a larger amount of defects possibly caused by strong Ag-rGH and AgBr-rGH interactions [26]. Fig. 3b also shows that 10% rGH-AgBr@rGO exhibited an increased degree of disorder and number of isolated double bonds, ascribed to the presence of Ag [27]. The intensity of the 2D peak (2700 cm^{-1}) was not as high as that of the G peak, being increased for 10% rGH-AgBr@rGO compared to rGH and illustrating that the join of AgBr made the distance between the graphene layer and layer, and layer thickness became thinning [28].

The morphological and microstructural details of as-prepared samples were analyzed by FE-SEM and TEM. Fig. 4a and b show SEM images of pristine AgBr and AgBr@rGO, respectively, revealing that particles of the former (1–1.5 μm) exhibited pronounced uncontrollable agglomeration, whereas those of the latter exhibited controlled sizes between 500 and 600 nm, showing a more uniform distribution. Previously, AgBr has been successfully prepared by addition of cetyltrimethylammonium bromide [29] and microwave-assisted methods [30], with particle size control achieved in both cases. GO nanosheets became very thin for ultra-

sonic treatment. GO was mixed with $\text{Ag}(\text{NH}_3)_2\text{OH}$ before forming AgBr, preventing the agglomeration of AgBr from reducing the particle size of AgBr and making the particle size of AgBr more uniform. No rGO nanosheets were observed for AgBr@rGO (Fig. 4b) due to the low rGO content. On the one hand, treatment of the negatively charged GO surface with $\text{Ag}(\text{NH}_3)_2\text{OH}$ not only increased the electrostatic repulsion between GO layers, but also induced the reduction of GO to rGO with increasing pH [31]. On the other hand, the electrostatic interaction of $[\text{Ag}(\text{NH}_3)_2]^+$ with GO enabled full contact required for hybridization. The surface of AgBr@rGO was further analyzed by energy dispersive spectrometer (EDS) elemental mapping (Fig. S1), which showed that C and O elements (and thus, rGO) were uniformly distributed on the surface of AgBr microspheres [32].

Fig. 4c and d show SEM images of rGH and 10% rGH-AgBr@rGO, respectively, revealing that the 3D structure of rGH retained the large accessible [17] to get AgBr@rGO. The morphology and stability of AgBr@rGO were controlled to some extent in rGH-AgBr@rGO (Fig. 4d). The presence of rGO in AgBr@rGO not only prevented

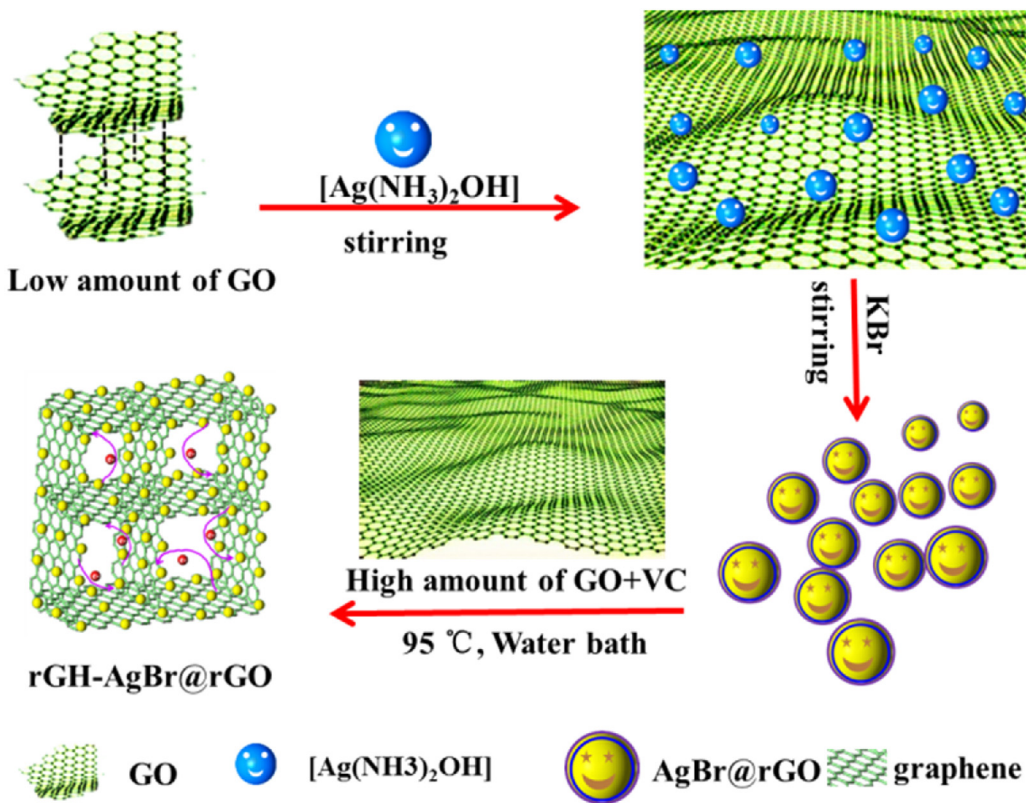


Fig. 5. Schematic synthesis of rGH-AgBr@rGO.

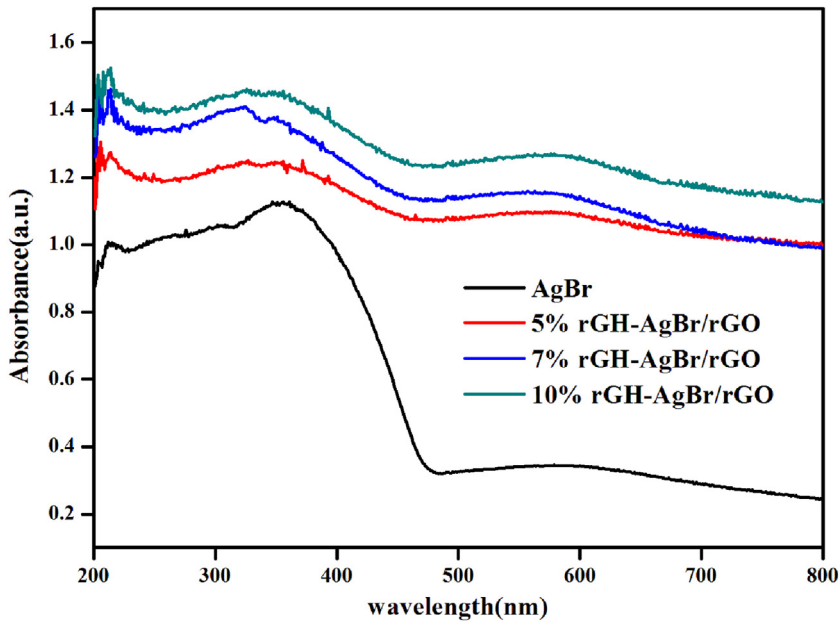


Fig. 6. UV-vis diffuse reflectance spectra of AgBr and rGH-AgBr@rGO.

VC from reducing Ag^+ to Ag^0 , avoiding the emergence of a large number of Ag particles (10–50 nm, Fig. 4d), but also changed the morphology of the graphene hydrogel, achieving a more regular and uniform particle size. Additionally, TEM imaging of GO (Fig. 4e) displayed that ultrasonication reduced the thickness of the GO film and achieved a homogenous distribution of AgBr, enabling particle size control in 10% rGH-AgBr@rGO (Fig. 4f). The overall process for

the fabrication of the rGH-AgBr@rGO is shown in Fig. 5. rGO as the film of the AgBr and the main skeletal support structure of the composite structure, it had great shape control, space filling, structural orientation and support structure [33,34].

UV-vis diffuse reflectance spectra of AgBr and rGH-AgBr@rGO composites are shown in Fig. 6, revealing that peaks related to charge transfer on the AgBr surface were progressively shifted to

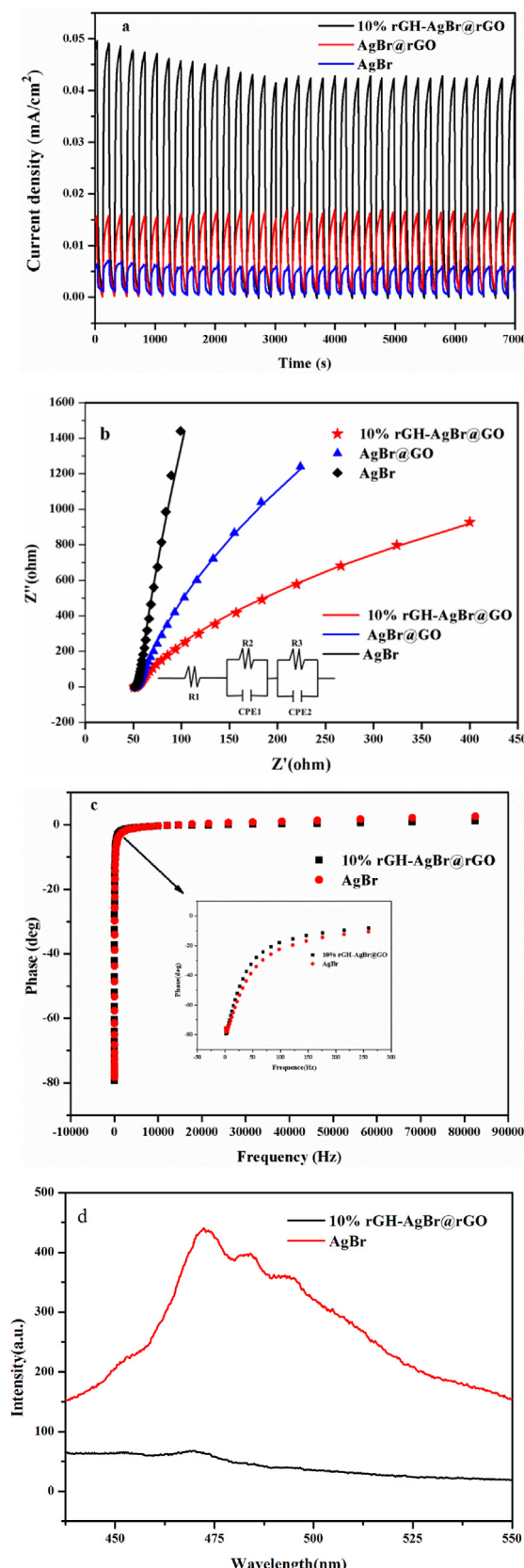


Fig. 7. (a) Transient photocurrent responses of pure AgBr, AgBr@rGO, and 10% rGH-AgBr@rGO. (b) EIS plots of samples irradiated with visible light. Inset: equivalent circuit used to fit the data. (c) Bode plot of pure AgBr and 10% rGH-AgBr@rGO. (d) PL spectra of AgBr and 10% rGH-AgBr@rGO.

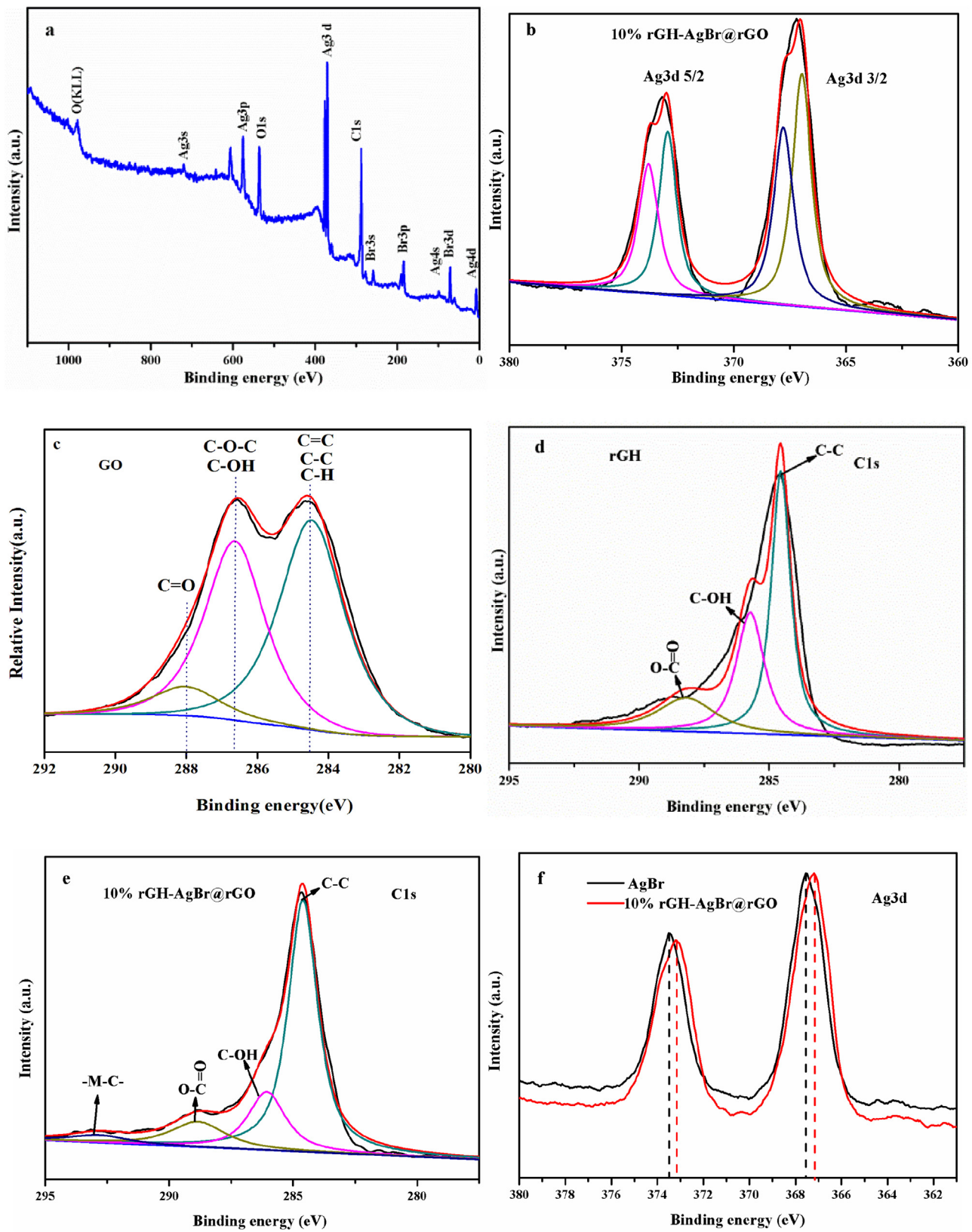


Fig. 8. XPS spectra of AgBr, GO, and 10% rGH-AgBr@rGO. (a) Survey spectrum, (b) Ag 3d spectrum of 10% rGH-AgBr@rGO. C 1s spectra of (c) GO, (d) rGH, and (e) 10% rGH-AgBr@rGO. (f) Ag 3d spectra of AgBr and 10% rGH-AgBr@rGO.

higher wavelengths at increased rGH loadings. Significant surface plasmon resonance (SPR) could be observed in the above spectra, indicating the presence of a small amount of Ag nanoparticles [35].

The photoelectrochemical performances of as-prepared samples are compared in Fig. 7(a), revealing that photocurrents of 10% rGH-AgBr@rGO and AgBr@rGO were significantly higher than

that of AgBr and confirming the excellent conductivity of rGO. The π - π conjugated structure of rGO could promote the transfer of photogenerated electrons and holes, improving their separation efficiency [15]. Under prolonged illumination, the photocurrent remained high despite a slight decrease, indicating that the addition of rGO makes AgBr more stable.

Fig. 7b shows typical EIS spectra of AgBr, AgBr@rGO, and 10% rGH-AgBr@rGO. ZSimpWin software was used to simulate an equivalent circuit (inset in Fig. 7b), where R_1 denotes the series resistance of the solution, R_2 is the resistive loss of the space charge layer, and R_3 stands for the charge transfer resistance in the Helmholtz layer, whereas CPE represents chemical capacitance [36]. Compared to pristine AgBr, rGH-AgBr@rGO and AgBr@rGO showed decreased arc radii, implying increased charge transfer rates due to hybridization with graphene and confirming the results obtained by analyzing Fig. 7a. Fig. 7c displays the inverse minimum frequency [37] of 10% rGH-AgBr@rGO and AgBr, located at 74.8 Hz and 82.1 Hz, respectively, revealing that the electron lifetime increased from 1.9 ms (AgBr) to 2.3 ms (10% rGH-AgBr@rGO), according to the formula $\tau \approx 1/(2\pi f)$ (where τ is the electron lifetime and f is the frequency) [38–40]. Thus, rGH inhibited the recombination of photogenerated electrons and holes, achieving improved charge separation efficiency and photocatalytic activity.

Charge separation efficiency was further tested by PL measurements (Fig. 7d) [41], revealing that the fluorescence intensity of pristine AgBr ($\lambda_{\text{max}} \sim 475$ nm) was much higher than that of 10% rGH-AgBr@rGO and further confirming that the addition of rGH successfully inhibited the recombination of electrons and holes [42].

The chemical states of elements and oxygen-containing functional groups of composites were investigated by XPS (Fig. 8) [43]. Fig. 8a presents a survey spectrum of 10% rGH-AgBr@rGO, with the region corresponding to Ag shown in Fig. 8b, revealing peaks of Ag^+ at 373 and 367 eV and those of Ag^0 at 374 and 367.9 eV which Ag^+ reached 71.5% through comparing the Ag^+ / Ag^0 and of the peak intensity ratio. Fig. 8c–e shows C 1s XPS spectra of GO, rGH, and 10% rGH-AgBr@rGO, respectively. The XPS spectrum of GO displays three peaks, ascribed to C–C, C=C, and C–H bonds (284.8 eV) C–O–C and C–OH bonds (286.5 eV), and carbonyl/carboxyl C=O

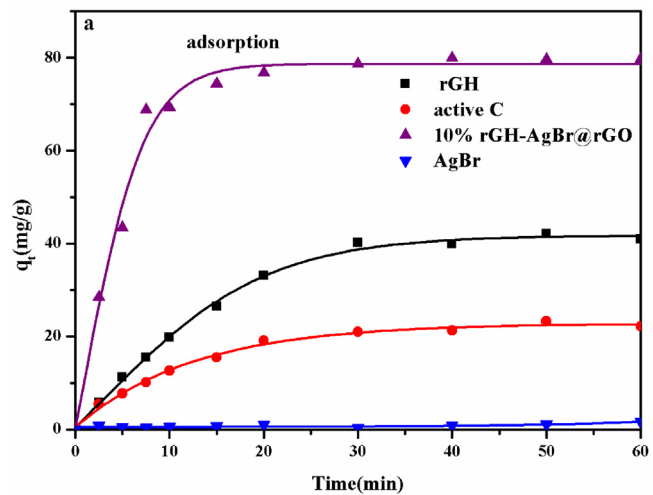


Fig. 9. Saturated adsorption capacities of different materials.

bonds (288.9 eV) [44,45]. In rGH, the intensity of these peaks was weakened due to VC-induced reduction. The normalized fractions of C–C peaks in Fig. 8c–e equaled 19.7, 50.7, and 67.6%, whereas the corresponding fractions of C=O bonds were reduced, indicating the progressing reduction of GO. Moreover, a new peak at 292.8 eV appeared in Fig. 8e, showing that AgBr was covalently bonded to graphene (i.e., hybridized with rGO) [46,47]. Similar conclusions were drawn by analysis of Fig. S1. Finally, hybridization also was confirmed by the binding energy change of Ag 3d peaks in the XPS spectra of complexed and pristine AgBr (Fig. 8f) [46].

Fig. 9 shows the saturated adsorption capacities of different catalysts with respect to BPA, showing that the amount of adsorbed BPA rapidly increased within 10 min for all materials except AgBr, followed by saturation after 30 min. The amounts of BPA adsorbed at saturation equaled 0.8, 22.2, 40.9, and 80.1 mg/g for AgBr, AC, rGH, and 10% rGH-AgBr@rGO, respectively. Abundant micropores of rGH enabled fast BPA transport to the catalytically active composites, greatly decreasing the time required to reach saturated adsorption [48]. 10% rGH-AgBr@rGO adsorbed the largest amount

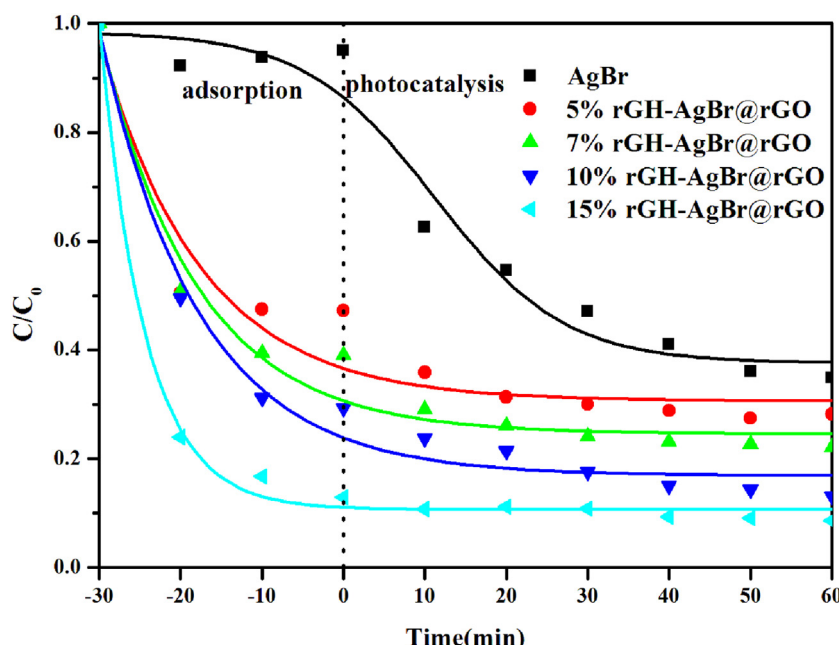


Fig. 10. Adsorption/photocatalytic degradation of BPA by different rGH-AgBr@rGO composites.

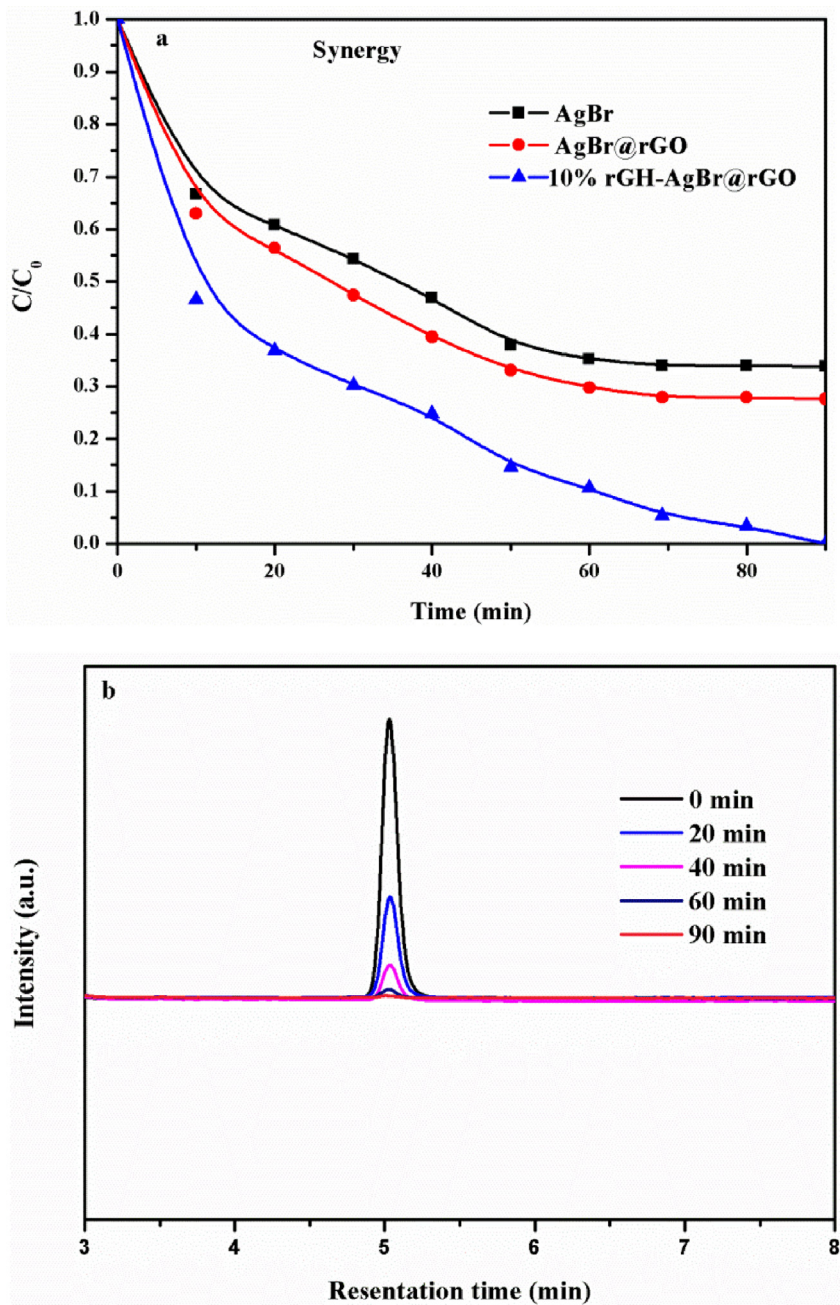


Fig. 11. (a) Results of adsorption/photocatalysis synergy tests of different materials. (b) HPLC chromatograms recorded at various reaction times for 10% rGH-AgBr@rGO.

of BPA at saturation, which may be ascribed to the AgBr nanoparticles contained in the rGH film, which result in different degrees of tearing between rGH membranes, thereby providing more adsorption sites. There was also proved by the increase BET surface area (SI: 180 m²/g to 220 m²/g; Fig. S2). The kinetics of BPA adsorption and degradation can be described as follows.

$$\ln(q_e - q_t) = \ln q_e - k_1 t \quad (1)$$

$$\frac{t}{q_t} = \frac{1}{k_2 q_e^2} + \frac{t}{q_e} \quad (2)$$

Where q_e (mg/g) and q_t (mg/g) are the amounts of BPA adsorbed on graphene at equilibrium and at time t (min), respectively, and k_1 (g/(mg min)) and k_2 (g/(mg min)) are the pseudo-first- and pseudo-second-order rate constants, respectively.

The adsorption mechanism was studied using 50 mL of a 20 ppm BPA solution and 0.1 g of 10% rGH-AgBr@rGO, and the obtained data were fitted by pseudo-first-order (Eq. (1)) and pseudo-second-order models (Eq. (2)) [49–51], with the obtained kinetic parameters and correlation coefficients (R^2) summarized in Table 1. The pseudo-second-order kinetic fit showed good agreement with experimental results, exhibiting an R^2 value above 0.99. π - π interactions of rGH and BPA may also contribute to fast adsorption, which is a prerequisite for the synergy of adsorption and photocatalysis [50]. In addition, different adsorption isotherm models were used to fit experimental results (SI, Table S1, Fig. S3, Eqs. S1 and S2). The Langmuir model described experimental results better than the Freundlich model, the maximum adsorption of 201 mg/g manifested the rGH adsorption on surface, single molecular layer adsorption and adsorption occurred in the homogeneous surface.

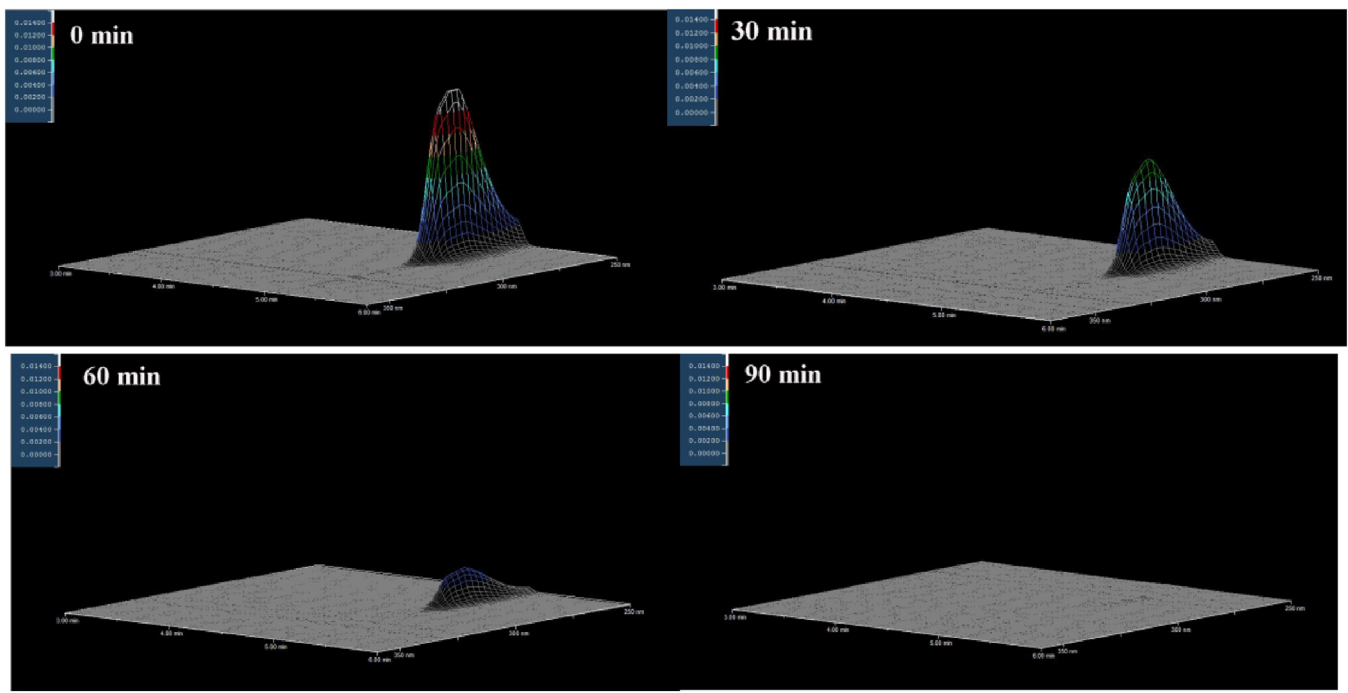


Fig. 12. 3D HPLC chromatographic characterization of BPA degradation.

Table 1
Kinetic parameters of BPA adsorption on 10% rGH-AgBr@rGO.

Q _{e(exp)}	pseudo-first-order			pseudo-second –order		
	k ₁	Q _{e(cal)}	R ²	k ₂	Q _{e(cal)}	R ²
80.6 mg/g	0.094 g/(mg min)	36.8 mg/g	0.83	0.0036 g/(mg min)	86.2 mg/g	0.99

Table S2 and Equations S3 and S4 reveal that adsorption of BPA by 10% rGH-AgBr@rGO was a spontaneous process, not requiring an additional driving force and being closely related to the π - π conjugation of rGH.

Fig. 10 illustrates the adsorption/photocatalytic degradation of BPA with the composites of different rGH ratios. The adsorption equilibrium was reached within 30 min, with BPA adsorption percentages equaling 5.0, 52.7, 60.9, 70.6, and 87.2% for AgBr, 5, 7, 10, 15% rGH-AgBr@rGO, respectively, reflecting the increased proportion of rGH, which manifested the adsorption effects of BPA mainly through π - π conjugation between graphene and BPA. BPA photocatalytic degradation percentages of 64.7, 71.8, 77.8, 86.9, and 91.4%, were observed for AgBr, 5, 7, 10, 15% rGH-AgBr@rGO, respectively. Although the compounds degradation rate were higher than the monomer, compounds were not as AgBr in terms of the overall rate of degradation, which may be due to the increasing rGH with increasing graphene content at the AgBr surface or at the junction of the nanoparticles so that lost a part of the visible-light irradiation [52].

Fig. 11a shows that the obtained composites could completely degrade BPA (50 mL, 20 ppm) due to the synergistic effect of adsorption and photocatalysis, although the degradation rates exhibited by pristine compounds were faster than those of composites. Since the photocatalytic degradation ability was almost completely lost at rGH contents above 10 wt.%, we did not study composites containing more than 15 wt.% rGH [53]. Fig. 11b shows HPLC chromatograms of BPA solutions, revealing that the area of the peak with a retention time of \sim 5 min gradually decreased with time, being reduced to zero after 90 min and indicating the complete degradation of BPA into small molecules [46], as confirmed by the absence of other peaks in HPLC chromatograms at 250–360 nm in

Fig. 12, which also implied the complete degradation of BPA into small molecules.

Fig. 13a illustrates the degradation of BPA by 10% rGH-AgBr@rGO under different conditions, with 100% degradation achieved by synergistic adsorption/photocatalysis, indicating the superiority of this environmental purification method to isolated photocatalysis or adsorption methods. Fig. 13b shows the results obtained for BPA degradation by 10% rGH-AgBr@rGO and 10% rGH-AgBr, revealing that the presence of hybridized AgBr@rGO not only accelerates the rate of electron/hole separation, but also reduces the photocorrosion of AgBr [54].

Fig. 14a compares the adsorption and photocatalytic degradation of BPA (50 mL, various concentrations) by 10% rGH-AgBr@rGO (0.1 g), revealing that the degradation degree decreased (86.8, 79.2, and 67.2%) with increasing BPA concentration (20, 40, and 60 ppm, respectively). This can be explained by the constant adsorption capacity of 10% rGH-AgBr@rGO, which results in a large amount of non-adsorbed BPA at high concentrations. Herein, the more the amount of photocatalytic degradation was needed so that the increase of the base would lead to the lower photocatalytic degradation rate. More importantly, these results imply that the composite still exhibited a certain photocatalytic activity at a high concentration of BPA, further illustrating the broad application range and practical value of 10% rGH-AgBr@rGO prepared by chemical reduction. Fig. 14b shows the cycling stability of 10% rGH-AgBr@rGO, with a 400 mesh strainer filter (38 μ m) used in each cycle. The filtered catalyst was not washed or dried before the next reaction. In the first cycle, 70.6% of BPA was removed, with lower values of 47.7 and 12.8% observed in the second and fifth cycles under adsorption-only conditions. The pollutant removal efficiency dropped from 100% in the first cycle to 90.1% in the

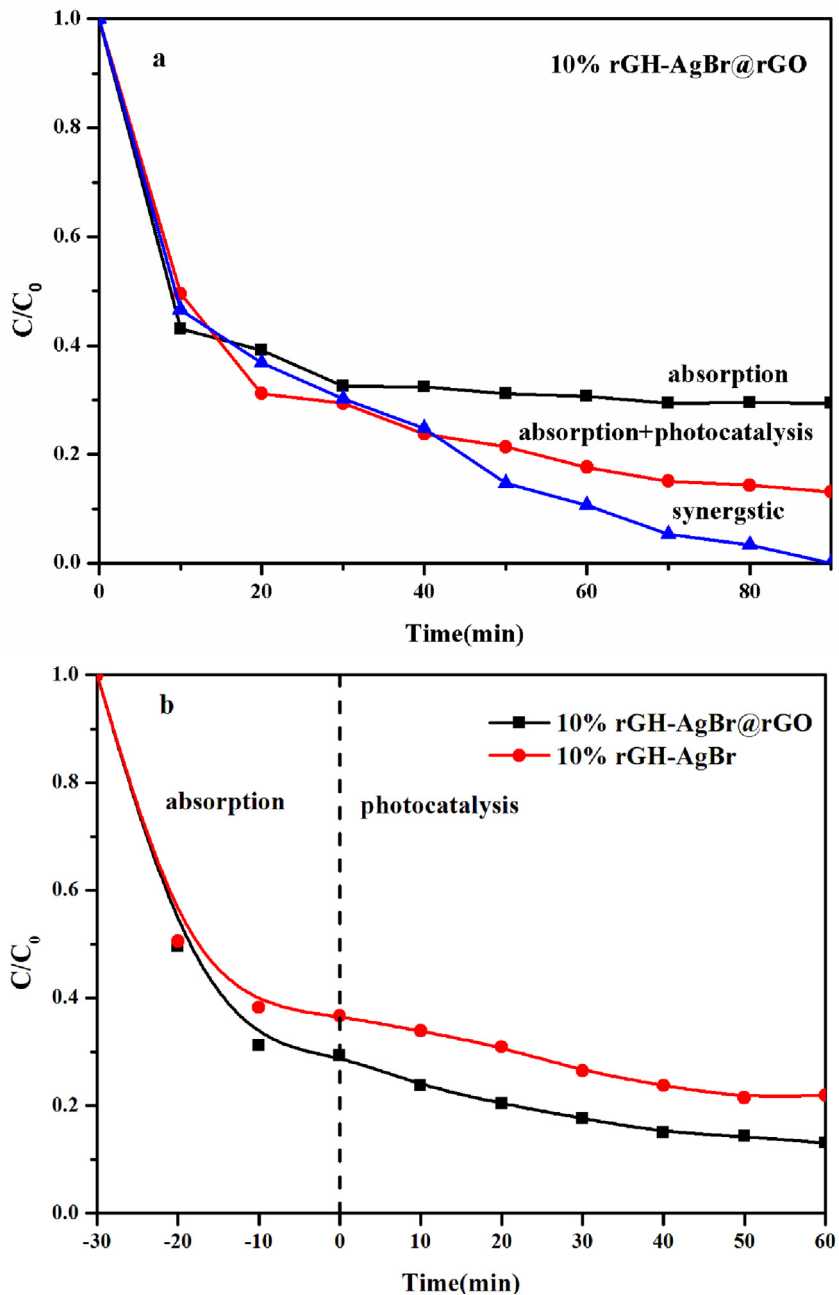


Fig. 13. (a) Degradation of BPA under different conditions. (b) Adsorption/photocatalytic degradation of BPA by 10% rGH-AgBr@rGO and 10% rGH-AgBr.

fifth cycle, indicating that the sample adsorption capacity was limited under synergistic adsorption/photocatalysis conditions, and the target contaminant was enriched on the surface of the sample while BPA cannot be completely degraded. Thus, synergistic adsorption/photocatalysis was demonstrated to be a more efficient means of environmental purification compared to adsorption only, due to the rapid light-induced mineralization of target contaminants adsorbed on the catalyst surface [55,56]. The thus achieved removal of target pollutants from the catalyst surface enabled further adsorption-degradation-desorption cycles.

As shown in Fig. 15a, the characteristic peaks of 10% rGH-AgBr@rGO remained largely unchanged after the stability test, although a new weak peak was detected at 38.1° , assigned to the (111) plane of Ag. Thus, the obtained results further confirmed that hybridization of graphene with AgBr and the reticular structure of rGH improved photocatalyst stability [54]. Fig. 15b and c depict SEM

images of 10% rGH-AgBr@rGO before and after synergistic absorption/photocatalysis, respectively, revealing almost no changes of AgBr particle morphology and pore structure, and showing that the addition of graphene to AgBr not only improved the photocatalytic properties of AgBr under visible-light irradiation, but also greatly reduced the amount of Ag [54].

The performance of rGH-AgBr@rGO in adsorption-based BPA removal was investigated for a dynamic system. Fig. 16 shows that breakthrough times of 3, 4, and 5 h were observed for rGH loadings of 5, 7, and 10%, respectively, since the increased surface area observed at higher loadings provided more sites for BPA adsorption. In addition, saturation of BPA adsorption was observed after 42, 44, and 45 h for 5%, 7%, and 10% rGH-AgBr@rGO, respectively, owing to the 3D structure of the graphene hydrogel and different diameter of the pore distribution in everywhere. Thus, high pore

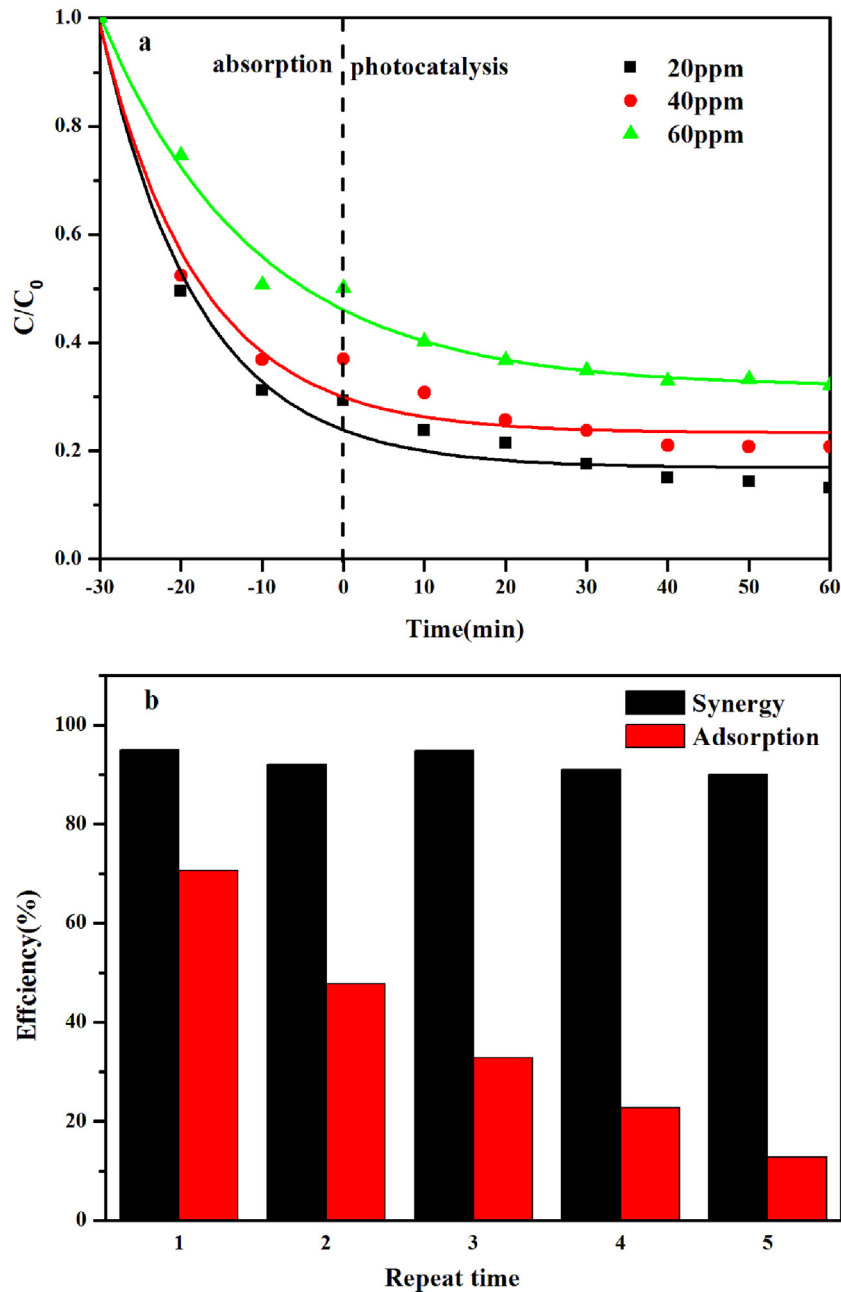


Fig. 14. (a) Photocatalytic degradation of BPA by 10% rGH-AgBr@rGO at different concentrations. (b) Cycling stability of 10% rGH-AgBr@rGO under different conditions.

volume resulted in a larger adsorbent capacity, facilitating the rapid progress of adsorption [57].

To determine the effect of different conditions, a 0.5 g sample of 10% rGH-AgBr@rGO was investigated at the same flow rate in Fig. S4, revealing that the degree of adsorption reached 100% in the first 5 h in the case of pure adsorption, while the breakthrough time for synergistic adsorption/photocatalysis was delayed by 1 h (i.e., equaling 6 h). Therefore, it was concluded that adsorption played a dominant role at the initial stage, and the effect of synergy manifested itself in increased breakthrough time, whereas the degradation of adsorption capacity exhibited a sharp decrease. The degree of BPA degradation reached 39.7% after 47 h (with adsorption equilibrium established after 40 h), indicating that the prepared composite exhibited a long working time and excellent degradation performance. Fig. S5 illustrates the performance of 10% rGH-AgBr@rGO during alternating dark-light cycling under contin-

uous flow conditions. When the BPA adsorption equilibrium was established under adsorption/photocatalytic synergy conditions, illumination was turned off, resulting in a rapid drop of BPA degradation degree to 0%. However, the removal ability could be quickly recovered when the lamp was turned back on. Moreover, the above figure shows that 10% rGH-AgBr@rGO could achieve a degradation degree of 39.6% after 70 h, revealing that this composite enabled stable synergistic adsorption/photocatalysis [17].

Trapping experiments were employed to detect the active species formed during the photocatalytic degradation of BPA and thus determine the reaction mechanism. Fig. 17 shows that $\cdot\text{OH}$, $\cdot\text{O}_2^-$, and holes (h^+) were detected using isopropanol (0.05 mL in 50 mL 20 ppm BPA), N_2 , and EDTA-2Na (0.05 g in 50 mL 20 ppm BPA) as trapping agents, respectively, revealing that $\cdot\text{OH}$ was not the main active species, since the addition of isopropanol did not significantly inhibit the photocatalytic reaction [52,58]. Conversely, in

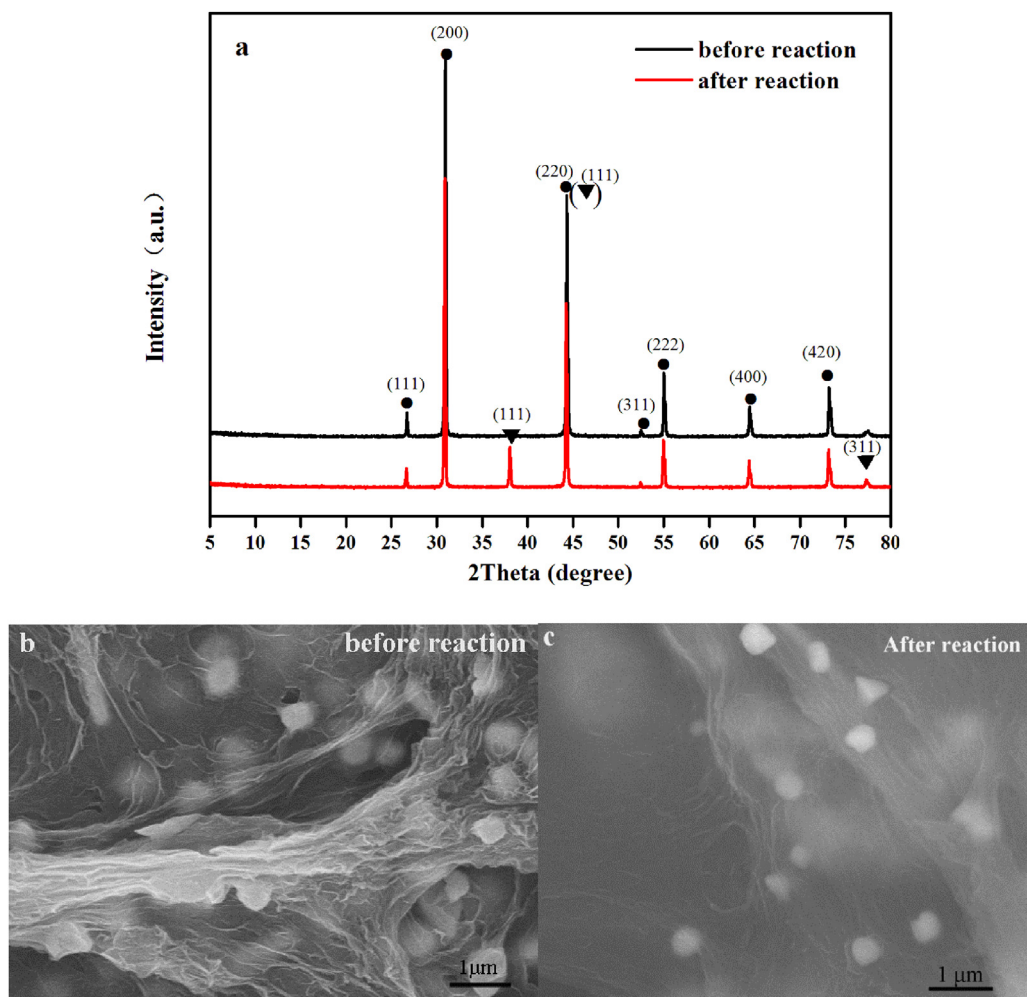


Fig. 15. (a) XRD spectra of 10% rGH-AgBr@rGO before and after recycling; SEM images of 10% rGH-AgBr@rGO before (b) and after (c) the catalytic reaction.

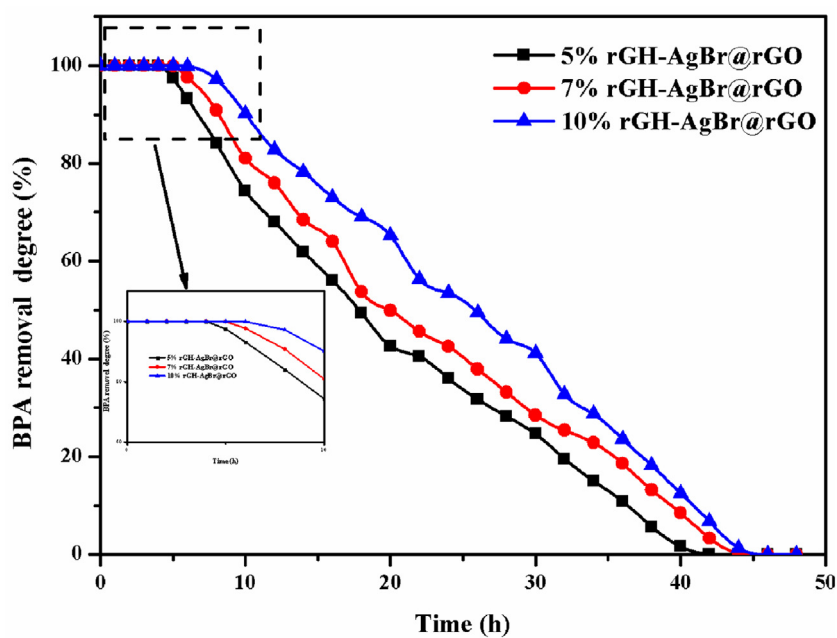


Fig. 16. Fraction of BPA (10 ppm) removed by 0.5 g samples of rGH-AgBr@rGO with different rGH loadings based on an adsorption-only mechanism (flowing phase).

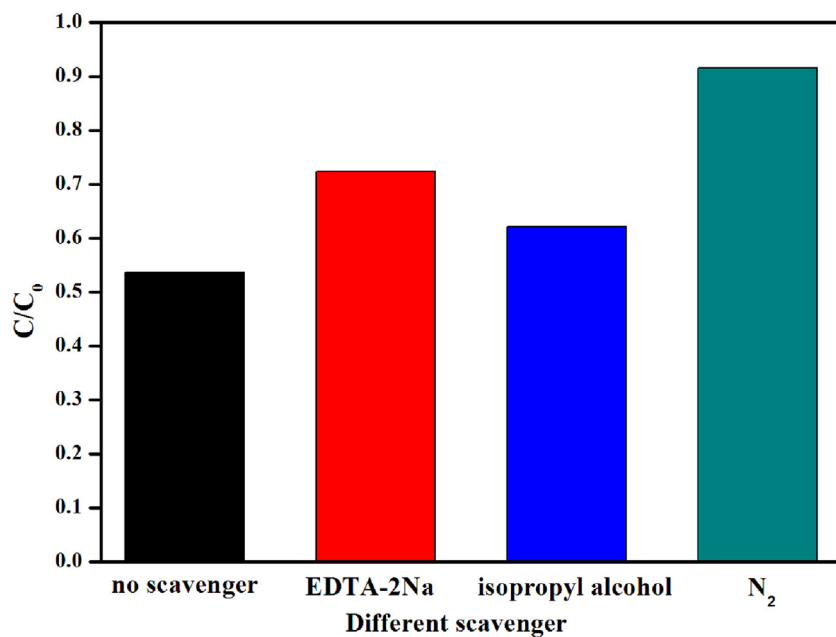


Fig. 17. Change of BPA photocatalytic degradation degree observed for 7% rGH-AgBr@rGO under visible-light irradiation in the presence of various trapping agents.

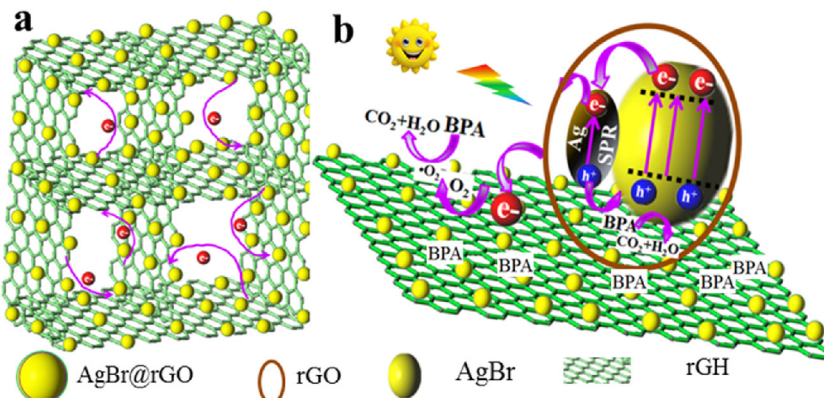


Fig. 18. Proposed mechanism for photocatalytic BPA degradation by rGH-AgBr@rGO under visible-light illumination.

the case of N_2 , the BPA degradation degree declined to 8.5% (degradation degree for catalyst-only solution equaled 49.5%), indicating that $\cdot O_2^-$ was the main active species involved in the photocatalytic process. In addition, the photocatalytic degradation efficiency was reduced by 20% in the presence of EDTA-2Na, indicating that h^+ also played a significant role in the above reaction.

The experimental results showed that rGH-AgBr@rGO exhibited a higher synergistic effect of adsorption and photocatalysis activity for BPA degradation than pristine AgBr. Based on the above analysis, a mechanism for the photocatalytic degradation of BPA by rGH-AgBr@rGO was proposed (Fig. 18), with both Ag and AgBr nanoparticles generating electrons and holes under irradiation by visible light. The produced holes directly reacted with BPA or surrounding water molecules (to produce $\cdot OH$), resulting in pollutant degradation. Owing to the quick charge transfer mediated by rGO, the photogenerated electrons moved to its surface due to hybridization, being further transferred to the rGH surface to react with O_2 and generate $\cdot O_2^-$. In general, most holes and electrons underwent fast recombination, with only a small part of them being involved in photocatalytic degradation, resulting in low quantum efficiency. However, rGH could effectively suppress the above recombination, extending the lifetime of photogenerated electrons. Moreover, $\pi-\pi$ conjugation enabled the adsorption of BPA on the surface of

rGH, resulting in much higher photocatalytic activity of the synthesized composites compared to that of AgBr due to the synergy of adsorption and photocatalysis.

4. Conclusions

AgBr was encapsulated by graphene to form AgBr@rGO, which was incorporated into a graphene gel system to form a graphene hydrogel (rGH-AgBr@rGO) with a 3D network structure. The core-shell structure of AgBr@rGO inhibited the growth of AgBr particles, achieving a controlled particle size of 500–600 nm, while hybridization with graphene promoted the rapid migration and separation of photogenerated charges. The 3D-structured graphene nanosheets of rGH-AgBr@rGO could rapidly adsorb organic contaminants, which were rapidly degraded under visible-light irradiation by AgBr@rGO nanoparticles. Moreover, 10% rGH-AgBr@rGO exhibited a superior synergy of photocatalytic and adsorption degradation activities, achieving 1.5-fold higher BPA removal degrees than pure AgBr. Cycling stability experiments revealed that 10% rGH-AgBr@rGO could achieve a BPA degradation degree of 90% after five repeated cycles. Moreover, under continuous flow conditions, the degree of BPA degradation was maintained at 100% in the first 6 h. Finally, the micron-sized 3D mesh structure could be recycled

using a simple filter without the use of complex catalyst filtration systems.

Thus, we have succeeded in preparing a stable and recyclable catalyst for the removal of BPA, which can be used in applications such as waste water treatment, paving a new way for the mitigation of environmental problems.

Acknowledgements

This work was financially supported by the National Natural Science Foundation of China (No. 51672081), Key Program of Natural Science of Hebei Province (B2016209375), Hebei Natural Science Funds for the Joint Research of Iron and Steel (B2016209348), Hebei Provincial Foundation for International cooperation (15391403D).

Appendix A. Supplementary data

Supplementary data associated with this article can be found, in the online version, at [10.1016/j.apcatb.2017.05.078](https://doi.org/10.1016/j.apcatb.2017.05.078).

References

- [1] H. Moriwaki, Y. Akaishi, M. Akamin, H. Usami, *Appl. Catal. B: Environ.* 204 (2017) 456–464.
- [2] S. Ikegami, H. Hamamoto, *Chem. Rev.* 109 (2009) 583–593.
- [3] N. Zhang, M.Q. Yang, S.Q. Liu, Y.G. Sun, Y.J. Xu, *Chem. Rev.* 115 (2015) 10307–10377.
- [4] X.T. Zhang, Z.Y. Sui, B. Xu, S.F. Yue, Y.J. Luo, W.C. Zhan, B. Liu, *J. Mater. Chem.* 21 (2011) 6494–6497.
- [5] H. Tang, P.B. Gao, Z.H. Bao, B. Zhou, J. Shen, Y.F. Mei, G.M. Wu, *Nano Res.* 8 (2015) 1710–1717.
- [6] Z. Xu, Y. Zhang, P.G. Li, C. Gao, 6 (2012) 7103–7113.
- [7] B.C. Qiu, M.Y. Xing, J.L. Zhang, *J. Am. Chem. Soc.* 136 (2014) 5852–5855.
- [8] Y.Q. He, Y. Liu, T. Wu, J.K. Ma, X.R. Wang, Q.J. Gong, W.N. Kong, F.B. Xing, Y. Liu, J.P. Gao, *J. Hazard. Mater.* 260 (2013) 796–805.
- [9] X.W. Zhao, B. Hu, J.J. Ye, Q. Jia, *J. Chem. Eng. Data* 58 (2013) 2395–2401.
- [10] J.P. Zhao, W.C. Ren, H.M. Cheng, *Mater. Chem.* 22 (2012) 20197–20202.
- [11] M.J. Kale, T. Avanesian, P. Christopher, *ACS Catal.* 4 (2014) 116–128.
- [12] K. Mondal, A. Sharma, *RSC Adv.* 6 (2016) 83589–83612.
- [13] K.I. Bolotina, K.J. Sikesb, Z. Jiang, M. Klimac, G. Fudenberg, J. Honec, P. Kima, H.L. Stormera, *Solid State Commun.* 146 (2008) 351–355.
- [14] R. Bera, S. Kundu, A. Patra, *ACS Appl. Mater. Interfaces* 24 (2015) 13251–13259.
- [15] X.J.B.L. Wang, Y.F. Zhu, *ACS Catal.* 2 (2012) 2769–2778.
- [16] T.G. Xu, L.W. Zhang, H.Y. Cheng, Y.F. Zhu, *Appl. Catal. B: Environ.* 101 (2011) 382–387.
- [17] Y. Li, W.Q. Cui, L. Liu, R.L. Zong, W.Q. Yao, Y.H. Liang, Y.F. Zhu, *Appl. Catal. B: Environ.* 199 (2016) 412–423.
- [18] W.J. Jiang, Y.F. Liu, J. Wang, M. Zhang, W.J. Luo, Y.F. Zhu, *Adv. Mater. Interfaces* 3 (2016) 1–9.
- [19] X.M. Tu, S.L. Luo, G.X. Chen, J.H. Li, *Chem. Eur. J.* 18 (2012) 14359–14366.
- [20] C. Cui, S. Li, Y.W. Qiu, H.H. Hu, X.Y. Li, C.R. Li, J.K. Gao, W.H. Tang, *Appl. Catal. B: Environ.* 200 (2017) 666–672.
- [21] M.S. Zhu, P.L. Chen, M.H. Liu, *Langmuir* 28 (2012) 3385–3390.
- [22] C.Y. Zeng, M. Guo, B.Z. Tian, J.L. Zhang, *Chem. Phys. Lett.* 575 (2013) 81–85.
- [23] D.A. Reddy, J. Choi, S. Lee, R. Ma, T.K. Kim, *RSC Adv.* 5 (2015) 67394–67404.
- [24] Z.Y. Gao, N. Liu, D.P. Wu, W.G. Tao, F. Xu, K. Jiang, *Appl. Surf. Sci.* 258 (2012) 2473–2478.
- [25] Y.Y. Fan, W.G. Ma, D.X. Han, S.Y. Gan, X.D. Dong, L. Niu, *Adv. Mater.* 27 (2015) 3767–3773.
- [26] Y. Gogotsi, J.A. Libera, N. Kalashnikov, M. Yoshimura, *Science* 290 (2000) 317–320.
- [27] K. Hareesh, R.P. Joshi, D.V. Sunitha, V.N. Bhoraskar, S.D. Dhole, *Appl. Surf. Sci.* 389 (2016) 1050–1055.
- [28] W.Q. Zha, W. Chen, Y.N. Yue, S.J. Wu, *Appl. Therm. Eng.* 113 (2017) 481–489.
- [29] L. Liu, S.L. Lin, J.S. Hu, Y.H. Liang, W.Q. Cui, *Appl. Surf. Sci.* 330 (2015) 94–103.
- [30] J. Jiang, H. Li, L.Z. Zhang, *Chem. Eur. J.* 18 (2012) 6360–6369.
- [31] J.Y. Hong, B.M. Bak, J.J. Wie, J. Kong, H.S. Park, *Adv. Funct. Mater.* 25 (2015) 1053–1062.
- [32] W.Q. Cui, W.J. An, L. Liu, J.S. Hu, Y.H. Liang, *J. Hazard. Mater.* 280 (2014) 417–427.
- [33] Y.Y. Sun, W.H. Zhang, D.S. Li, L. Gao, C.L. Hou, Y.H. Zhang, Y.Q. Liu, *J. Alloys Compd.* 649 (2015) 579–584.
- [34] S. Vadahanambi, S.H. Lee, W.J. Kim, I.K. Oh, *Environ. Sci. Technol.* 47 (2013) 10510–10517.
- [35] H. Zhang, X.F. Fan, X. Quan, S. Chen, H.T. Yu, *Environ. Sci. Technol.* 45 (2011) 5731–5736.
- [36] S.M. Sun, W.Z. Wang, L. Zhang, *J. Phys. Chem. C* 117 (2013) 9113–9120.
- [37] H.W. Huang, X.W. Li, J.J. Wang, F. Dong, P.K. Chu, T.R. Zhang, Y.H. Zhang, *ACS Catal.* 5 (2015) 4094–4103.
- [38] H. Wang, Y.H. Liang, L. Liu, J.S. Hu, W.Q. Cui, *Appl. Surf. Sci.* 392 (2017) 51–60.
- [39] H.W. Huang, K. Liu, Y.L. Zhang, K. Chen, Y.H. Zhang, N. Tian, *RSC Adv.* 4 (2014) 49386–49394.
- [40] H.W. Huan, K. Xiao, Y. He, T.R. Zhang, F. Dong, X. Du, Y.H. Zhang, *Appl. Catal. B: Environ.* 199 (2016) 75–86.
- [41] S.J. Zhuo, M.W. Shao, S.T. Lee, *ACS Nano* 6 (2012) 1059–1064.
- [42] W.L. Shi, H.C. Lv, S.L. Yuan, H. Huang, Y. Liu, Z.H. Kang, *Sep. Purif. Methods.* 174 (2017) 75–83.
- [43] Z.J. Fan, B. Liu, J.Q. Wang, S.Y. Zhang, Q.Q. Lin, P.W. Gong, L.M. Ma, S.R. Yang, *Adv. Funct. Mater.* 24 (2014) 3933–3943.
- [44] L. Zhang, Q.H. Zhan, H.Y. Xie, J. Guo, H.L. Lyu, Y.G. Li, Z.G. Sun, H.Z. Wang, Z.H. Guo, *Appl. Catal. B: Environ.* 201 (2017) 470–478.
- [45] P.Z. Sun, M. Zhu, K.L. Wang, M.L. Zhong, J.Q. Wei, D.H. Wu, H.W. Zhu, *ACS Appl. Mater. Interfaces* 5 (2013) 9563–9571.
- [46] L. Liu, L. Ding, Y.G. Liu, W.J. An, S.L. Lin, Y.H. Liang, W.Q. Cui, *Appl. Catal. B: Environ.* 201 (2017) 92–104.
- [47] C. Gong, S. McDonnell, X.Y. Qin, A. Azcatl, H. Dong, Y.J. Chabal, K. Cho, R.M. Wallace, *ACS Nano* 8 (2013) 642–649.
- [48] Y. Shen, Q.L. Fang, B.L. Chen, *Environ. Sci. Technol.* 49 (2014) 67–84.
- [49] J. Xu, L. Wang, Y.F. Zhu, *Langmuir* 28 (2012) 8418–8425.
- [50] M. Nawaz, W. Miran, J. Jang, D.S. Lee, *Appl. Catal. B: Environ.* 203 (2017) 85–95.
- [51] M. Ziegmann, F.H. Frimmel, *Water Sci. Technol.* 61 (2010) 273–281.
- [52] A. Esmaili, M.H. Entezari, *J. Colloid Interface Sci.* 466 (2016) 227–237.
- [53] X.H. Meng, X. Shao, H.Y. Li, J. Yin, J. Wang, F.Z. Liu, X.H. Liu, M. Wang, H.L. Zhong, *Mater. Lett.* 105 (2013) 162–165.
- [54] M.S. Zhu, P.L. Chen, M.H. Liu, *Acs Nano*, 5 (2011) 4529–4536.
- [55] W. Liu, J.R. Ni, X.C. Yin, *Water Res.* 53 (2014) 12–25.
- [56] S.B. Wang, X.W. Zhan, L. Pan, F.M. Zhao, J.J. Zou, T. Zhang, L. Wang, *Appl. Catal. B: Environ.* 164 (2015) 234–240.
- [57] M. Karimi, A. Shojaei, A. Nematollahzadeh, M.J. Abdekhodaie, *Chem. Eur. J.* 210 (2012) 280–288.
- [58] M. Ge, H. Zheng, *Ceram. Int.* 42 (2016) 6510–6514.